Microstructural Deformations Within the Depth of the Lamina Cribrosa in Response to Acute In Vivo Intraocular Pressure Modulation

Yoav Glidai,[1] Katie A. Lucy,[1] Joel S. Schuman,[1–3] Palaiologos Alexopoulos,[1] Bo Wang,[4] Mengfei Wu,[1,5] Mengling Liu,[1,5] Jonathan P. Vande Geest,[4,6,7] Hirut G. Kollech,[8] TingFang Lee,[1,5] Hiroshi Ishikawa,[1] and Gadi Wollstein[1,3]

[1]Department of Ophthalmology, NYU Langone Health, New York, New York, United States
[2]Department of Biomedical Engineering, NYU Tandon School of Engineering, New York, New York, United States
[3]Center for Neural Science, NYU, New York, New York, United States
[4]UPMC Eye Center, Eye and Ear Institute, Department of Ophthalmology, University of Pittsburgh Medical Center, Pittsburgh, Pennsylvania, United States
[5]Division of Biostatistics, Departments of Population Health and Environmental Medicine, NYU Langone Health, New York, New York, United States
[6]Department of Bioengineering, University of Pittsburgh, Pittsburgh, Pennsylvania, United States
[7]McGowan Institute for Regenerative Medicine, University of Pittsburgh, Pittsburgh, Pennsylvania, United States
[8]Computational Modeling and Simulation Program, University of Pittsburgh, Pittsburgh, Pennsylvania, United States

Correspondence: Gadi Wollstein, Department of Ophthalmology, NYU Langone Health, 222 East 41st Street, New York, NY 10017, USA; gadi.wollstein@nyulangone.org.

Received: August 30, 2021
Accepted: April 26, 2022
Published: May 23, 2022

Citation: Glidai Y, Lucy KA, Schuman JS, et al. Microstructural deformations within the depth of the lamina cribrosa in response to acute in vivo intraocular pressure modulation. *Invest Ophthalmol Vis Sci.* 2022;63(5):25. https://doi.org/10.1167/iovs.63.5.25

Purpose. The lamina cribrosa (LC) is a leading target for initial glaucomatous damage. We investigated the in vivo microstructural deformation within the LC volume in response to acute IOP modulation while maintaining fixed intracranial pressure (ICP).

Methods. In vivo optic nerve head (ONH) spectral-domain optical coherence tomography (OCT) scans (Leica, Chicago, IL, USA) were obtained from eight eyes of healthy adult rhesus macaques (7 animals; ages = 7.9–14.4 years) in different IOP settings and fixed ICP (8–12 mm Hg). IOP and ICP were controlled by cannulation of the anterior chamber and the lateral ventricle of the brain, respectively, connected to a gravity-controlled reservoir. ONH images were acquired at baseline IOP, 30 mm Hg (H1-IOP), and 40 to 50 mm Hg (H2-IOP). Scans were registered in 3D, and LC microstructure measurements were obtained from shared regions and depths.

Results. Only half of the eyes exhibited LC beam-to-pore ratio (BPR) and microstructure deformations. The maximal BPR change location within the LC volume varied between eyes. BPR deformer eyes had a significantly higher baseline connective tissue volume fraction (CTVF) and lower pore aspect ratio ($P = 0.03$ and $P = 0.04$, respectively) compared to BPR non-deformer. In all eyes, the magnitude of BPR changes in the anterior surface was significantly different (either larger or smaller) from the maximal change within the LC (H1-IOP: $P = 0.02$ and H2-IOP: $P = 0.004$).

Conclusions. The LC deforms unevenly throughout its depth in response to IOP modulation at fixed ICP. Therefore, analysis of merely the anterior LC surface microstructure will not fully capture the microstructure deformations within the LC. BPR deformer eyes have higher CTVF than BPR non-deformer eyes.

Keywords: lamina cribrosa (LC), optical coherence tomography (OCT), intraocular pressure (IOP)

The lamina cribrosa (LC) is a collagen fiber meshwork within the optic nerve head (ONH) with a reported ex vivo range of average thickness of 115 to 273 µm[1] and in vivo average thickness of 335 ± 3.9 µm, in non-human primates.[2] As the unmyelinated retinal ganglion cells axons exit the eye, the LC provides them structural and nutrient support.[3–5] The crucial role of the LC in the pathogenesis of glaucomatous optic neuropathy has been well established,[6–8] but the exact mechanism of assault has yet to be determined. Considering that the LC is roughly one-third the thickness of the sclera and that its load-bearing components comprise only about 40% of its volume, it is regarded as a biomechanical weak spot of the globe.[9–11] Pressure-induced deformation of the LC triggers events, such as compromised axoplasmic flow, reduced vascular perfusion, and astrocyte activation, which all contribute to the development of glaucomatous optic neuropathy.[12–15]

Advances in optical coherence tomography (OCT) have led to renewed interest in studying the LC in vivo, as high-quality, detailed scans visualizing its 3D microarchitecture

Investigative Ophthalmology & Visual Science

are now available.[16,17] Several studies, both in vivo and ex vivo, have shed light on the LC structure and deformation in humans and animal models.[18–23] LC macro- (i.e. thickness and depth)[24–28] and micro-structure (pores and beams)[18] parameters were reportedly associated with glaucoma.

Most studies conducted so far on the LC in vivo primarily focused on the anterior laminar surface.[29–34] However, as the LC is a complex 3D structure, we propose that the entire LC volume, not solely the anterior surface, be considered when evaluating its role in glaucoma pathogenesis. In this study, we assess the in vivo 3D deformation of the LC microstructure in response to acute IOP modulation while maintaining a fixed intracranial pressure (ICP) using a non-human primate model. In addition, we examine if anterior LC deformations are representative of deformations occurring within the lamina depth. We hypothesize that an analysis limited to the anterior LC surface is insufficient to fully explore the acute LC dynamics and the consequent insult to the trespassing optic nerve axons.

Methods

Animals

Adult, healthy, rhesus macaque monkeys (Macaca mulatta) participated in this study. The animals previously participated in other nonrelated experiments that did not affect their eyes, brain, circulation, or immune system. All experimental procedures were approved by the University of Pittsburgh's Institutional Animal Care and Use Committee (IACUC) and adhere to both the National Institute of Health's Guide for the Care and Use of Laboratory Animals and the Association of Research in Vision and Ophthalmology (ARVO) statement for the use of animals in ophthalmic and vision research. Monkeys were given access to free water and a variety of enrichments daily, which included visual, audio, taste, and textures, and encouraged normal primate behavior of grooming and foraging.

Experimental Design

The animals were anesthetized and placed on a surgical table with their head in an upright position and their body prone. A small craniotomy was performed, through which a lumbar catheter (Medtronic, Minneapolis, MN, USA) was inserted into the lateral ventricle. ICP was gravity controlled by connecting the catheter to a saline reservoir. ICP was also monitored by a fiberoptic pressure sensor inserted into the brain's parenchyma (ICP EXPRESS monitoring system; DePuy Synthes, Raynham, MA, USA). The pressure transducer was calibrated before the use by submerging into saline. ICP was maintained at the opening pressure of each animal ranging between 8 and 12 mm Hg. Control of IOP was achieved by inserting a 27-gauge needle to the anterior chamber, connected to a separate saline reservoir, and adjusted by gravity control. IOP was adjusted to 3 pressure settings: 15 (N-IOP), 30 (H1-IOP), and 40 mm Hg (H2-IOP). The precision of the IOP and ICP values were within the range of ±1 mm Hg with fluid added or withdrawn to reach target pressure. In order to account for the viscoelastic effect caused by each pressure change, a 5-minute pause was imposed after each pressure change.[35] In each pressure setting, OCT scans of the ONH were acquired.

Anesthesia

Anesthesia was achieved with ketamine (20 mg/kg), midazolam (0.25 mg/kg), and maintained with isoflurane (1 ± 3%). The subjects were intubated and artificially ventilated to maintain an end-tidal CO_2 of 35 mm Hg for the duration of the experiment. To reduce movements during scanning, animals were paralyzed using vecuronium bromide (2 mg/hour). At the end of the experiment, euthanasia was induced using somnasol (Henry Schein, Melville, NY, USA) at a dosage of 85 mg/kg.

OCT Imaging

The pupils were dilated using tropicamide ophthalmic solution, 0.5% (Bausch & Lomb, Rochester, NY, USA). A rigid gas permeable contact lens (Boston EO, Boston, MA, USA) was fitted to improve the scan quality. The eyes were kept open using a wire speculum, and corneas were irrigated every 5 minutes. All eyes were scanned using a spectral-domain OCT device (Leica, Chicago, IL, USA) with a scan rate of 20,000 A-scans/second and a light source with a broadband superluminescent diode (Superlum, Dublin, Ireland; $\lambda = 870$ nm, $\Delta\lambda = 200$ nm). Two to four raster scans focused on the LC were acquired in each pressure setting using a scan pattern of 5 × 5 × 2 mm volume (512 × 512 × 1024 samplings).

Image Analysis

The scans were subjectively inspected, and those with poor LC microstructure visualization were excluded. The images were analyzed in 3D using a semi-automated method we previously described.[18,36] In brief, ImageJ was used for bicubic image interpolation to make the images isotropic. Images were aligned to make Bruch's membrane opening horizontal. Regions of visible LC microstructure were manually selected by a qualified operator masked to the microstructure analysis outcome. The best quality scans at each pressure setting were registered (translation and rotation) to each other by matching distinct structural features. Because of the irregular structure of the LC and in order to prevent the confounding effect related to the quantification of different LC areas in varying testing settings, only overlapping areas of visible LC among all settings for a given animal were analyzed. The analyzable lamina was reported as a percent from the Bruch's membrane opening. A straight plane was aligned to the anterior lamina surface and used as a reference plane to all subsequent measurements. A 3D automated segmentation algorithm in ImageJ was used to quantify beam thickness, pore diameter, and beam diameter to pore area ratio (BPR). Because the OCT device is optimized for human imaging and the optical properties of each monkey eye vary, LC measurements were adjusted based on eye-specific histology, as previously described.[2] Disc area and disc aspect ratio were measured by manually defining the Bruch's membrane opening using the ImageJ area calculation feature. The microstructure measurements were analyzed at each slice as continuous variables anteriorly to posteriorly. The mean pore area and aspect ratio (AR) were also calculated by ImageJ after pores were automatically segmented. Connective tissue volume fraction (CTVF) was calculated by dividing the area occupied with LC beams to the entire analyzed area.

To quantitively differentiate between eyes that exhibit deformation to those that did not, we computed the

absolute difference in BPR between each consecutive single pixel planes, for each eye. An arbitrarily defined threshold of 0.2 was used where eyes showing absolute difference exceeding 0.2 were defined as BPR deformer and those below 0.2 defined as BPR non-deformer. In order to examine if changes detected in the lamina surface can be used as a surrogate of changes occurring within the lamina, the BPR was averaged from five consecutive, most anterior, single pixel planes. This value was compared with five consecutive single pixel planes at regions within the LC depth that displayed the absolute maximum BPR change (either positive or negative) in response to IOP modulation.

Using our previously described procedure, we computed the displacement and deformation tensor in the 3D LC images.[37] Briefly, a digital volume correlation (DVC) algorithm was used to compute the displacement field between two image volumes at different pressure values.[38] Specifically, N-IOP versus H1-IOP and H1-IOP versus H2-IOP. The resulting displacement field was smoothed and principal stretch values of the right Cauchy stretch tensor were calculated using a modified script from the method developed and validated by Kroon[39] and Adb-Elmoniem et al.[40] Values of first principal stretch were isolated using binary masks for each slice corresponding to the slices studied. Due to computational resource limitations, the images were scaled down 20% from their original size. In each depth slice, values of the 95th and 5th percentile of principal strain were calculated and reported as the range of strain.

Statistical Analysis

Summary statistics were provided with mean and standard deviation. At the baseline IOP and ICP setting, a linear mixed-effects model with a random intercept to account for multiple frames per eye was used to test whether parameters differed between BPR deformer and BPR non-deformer eyes. Wilcoxon rank sum test was used to test whether the absolute percentage changes in BPR were different for the deformer versus the non-deformer eyes. Both high IOP and very high IOP settings were considered while fixing ICP at the baseline setting. Linear mixed-effect model was also used to determine the effect of depth on the difference from baseline in BPR for each single pixel plane while accounting for the animal age and with random intercept to account for multiple frames per eye. Association between the difference in BPR from the corresponding baseline measurement and strain values and strain range were analyzed by linear mixed-effects model adjusting for age with random intercept to account for multiple frames per eye. Statistical analysis was performed using R software version 3.5.2. A P value less than 0.05 was considered statistically significant.

Results

Eight eyes of seven healthy, adult, rhesus macaque monkeys (Macaca Mulatta) were included in the analysis (6 OD, 2 OS; 5 male and 2 female monkeys). Baseline characteristics, macro and microstructure measurements are detailed in Table 1. The size of the analyzable lamina as a percent from the Bruch's membrane opening ranged between 2.9 and 17.8%, per eye. The mean number of single-pixel thick enface slices analyzed per eye was 98 (range = 76–127), with a corresponding analyzable depth ranging between 148.2 and 247.7 µm.

Effect of IOP Modulation

Figure 1 demonstrates the effect of IOP at various levels (with fixed ICP) on BPR as a function of depth in all eyes. Half of the eyes (Figs. 1A–D) showed evident BPR-expressed deformation in response to IOP, whereas the rest did not (Figs. 1E–H). Using the quantitative method to determine BPR deformer and non-deformer groups, the BPR deformer eyes (eyes A–D) had an average absolute difference in BPR between consecutive single pixel planes of 0.48 ± 0.35 (range = 0.23–1.00), whereas in BPR non-deformer eyes (eyes E–H), the average was 0.16 ± 0.02 (range = 0.12–0.19) and the difference between the 2 groups was statistically significant ($P = 0.03$).

Among deformed eyes, 3 main patterns were noted: (1) increase in BPR at H1-IOP and H2-IOP, mainly at the anterior and middle depth regions of the LC with no deformation in the posterior lamina (see Figs. 1A, 1D), (2) increase in BPR that is most pronounced in the anterior and posterior segment of the lamina with normal BPR in the middle LC (see Fig. 1B), and (3) a marked increase in BPR that is limited to roughly the posterior third of the LC thickness (see Fig. 1C). In most eyes, higher IOP induced more pronounced deformation. One eye was an exception, where maximal deformation was noted in a lower increase in IOP with a similar but smaller magnitude of deformation in the higher IOP (see Fig. 1D).

Evaluating the effect on the pores and beams separately (Fig. 2) revealed several patterns. The rise in BPR at the anterior lamina in higher IOP (see Fig. 1A) resulted from increased beam thickness and decreased pore diameter, particularly in the anterior and middle lamina (see Fig. 2A). In Figure 2B, there is an anterior and posterior (but not in the middle) increase in beam thickness, with a reduction in pore diameter, corresponding to the BPR changes seen in Figure 1B. Figure 2C demonstrates an increase in beam thickness in the posterior half of the LC associated with pore diameter reduction in the posterior third, both occurring only at H2-IOP, leading to increased posterior BPR (see Fig. 1C). In Figure 2D, a marked increase in beam thickness in the anterior LC occurs with a moderate decrease in pore diameter, producing the BPR increase at the anterior LC (see Fig. 1D).

A comparison of baseline ONH characteristics and LC microstructure between eyes that exhibited BPR deformation (eyes A–D) and eyes that did not (eyes E–H) is shown in Table 1. BPR deformers had a significantly higher baseline CTVF than BPR non-deformers (0.77 ± 0.04 vs. 0.68 ± 0.04, $P = 0.034$) (Supplementary figure 1). Furthermore, BPR deformers had lower baseline pore AR compared to eyes that did not (1.80 ± 0.15 vs. 1.93 ± 0.16, $P = 0.044$). Overall, baseline BPR was only marginally higher in BPR deformers compared to non-deformers (1.89 ± 0.29 vs. 1.46 ± 0.16, $P = 0.060$). We did not detect significant differences in age, optic disc size and AR, beam thickness, pore diameter, and pore area.

Change in BPR With Depth

Pooling data from all eyes to evaluate the effect of depth on BPR, it was noted that the substantially stronger magnitude of the effect in the eye of subject B, compared to all other eyes, distorted the statistical outcome. When the eye was included or omitted from the analysis, depth had a significant effect but in opposite directions and there-

Investigative Ophthalmology & Visual Science

Investigative Ophthalmology & Visual Science

Table 1. Baseline Characteristics of Eyes Included in This Study

Eye	NHP No.	OD/OS	Sex	Age	Disc Area, μm^2	Disc Aspect Ratio	Lamina Cribrosa Parameters					
							Beam Thickness, µm	Pore Diameter, µm	BPR	CTVF, %	Mean Pore Area, μm^2	Pore Aspect Ratio
A	11	OD	M	8.7	2.71	1.38	39.59 (2.55)	26.72 (2.01)	1.49 (0.09)	0.70 (0.01)	1067.94 (160.14)	1.82 (0.11)
B	2	OD	F	14.4	2.35	1.27	36.19 (0.97)	20.05 (1.07)	1.81 (0.09)	0.76 (0.02)	544.43 (70.51)	1.79 (0.17)
C	8	OD	M	9.7	2.67	1.33	43.87 (1.93)	22.10 (1.43)	1.99 (0.11)	0.79 (0.01)	669.73 (88.47)	1.88 (0.19)
D	5	OD	M	8.7	3.83	1.35	55.68 (2.75)	25.51 (2.44)	2.20 (0.18)	0.81 (0.02)	978.04 (188.46)	1.76 (0.06)
E	10	OD	M	11.2	2.34	1.37	42.03 (2.60)	24.73 (1.51)	1.70 (0.08)	0.74 (0.01)	843.87 (173.77)	1.91 (0.16)
F	6	OD	M	7.9	3.05	1.31	43.39 (4.54)	32.11 (2.79)	1.35 (0.06)	0.64 (0.01)	2152.23 (436.92)	2.00 (0.15)
G	1	OS	F	11.9	2.43	1.32	30.86 (1.64)	21.34 (0.91)	1.45 (0.05)	0.67 (0.01)	847.40 (136.64)	1.97 (0.14)
H	6	OS	M	7.9	3.05	1.32	43.35 (1.92)	32.28 (1.93)	1.35 (0.11)	0.66 (0.02)	1756.44 (357.03)	1.83 (0.11)
All eyes (SD)				10.05 (2.29)	2.80 (0.50)	1.33 (0.04)	41.87 (7.15)	25.61 (4.63)	1.67 (0.31)	0.72 (0.06)	1107.51 (557.64)	1.87 (0.09)
BPR deformers (SD)				10.38 (2.72)	2.89 (0.65)	1.33 (0.05)	44.49 (8.08)	23.69 (3.23)	1.89 (0.29)	0.77 (0.04)	823.73 (255.53)	1.80 (0.15)
BPR non-deformers (SD)				9.72 (2.13)	2.70 (0.37)	1.33 (0.03)	40.40 (5.84)	28.05 (5.05)	1.46 (0.16)	0.68 (0.04)	1460.96 (664.49)	1.93 (0.16)
BPR deformers vs. non-deformers, *P* value				0.66	0.89	0.66	0.48	0.27	0.06	0.03*	0.15	0.04*

"BPR deformers" group are eyes that displayed a BPR change in response to IOP elevation (A–D), whereas "BPR non-deformers" include eyes that did not (E–H). Results are reported as mean (SD).

NHP, non-human primate; BPR, beam-to-pore ratio; CTVF, connective tissue volume fraction.

fore this eye was not included in this part of the analysis. In both high and very high settings, depth had a negative (−0.0011 and −0.0003, respectively; deeper inside the lamina, smaller difference from the corresponding measurement at the baseline setting) and significant effect, that was markedly stronger in the high IOP setting ($P < 2e^{-16}$) than in the very high setting ($P = 0.008$). In both pressure settings, no significant effect was detected for age.

Do Anterior Lamina Deformations Represent Deeper Lamina Changes?

The depth of maximal BPR deformation (either positive or negative) varied between eyes, ranging from 25.3 to 202.8 µm from the anterior LC surface (see Fig. 1). In most cases, the maximum BPR change consisted of a negative peak (BPR became lower than the surface). The median absolute difference in BPR between the anterior surface of the lamina and the maximal deformation was 16.00% ± 12.80 and 19.85% ± 15.40, at H1-IOP and H2-IOP, respectively. In eyes that deformed, median absolute BPR change from the anterior surface was 24.25% ± 15.60 and 35.80% ± 14.20 at H1-IOP and H2-IOP, respectively. As expected, BPR non-deformer eyes showed lower median absolute BPR change between the anterior LC surface and the region of maximal deformation (15.35% ± 5.90 and 14.30% ± 3.40 at H1-IOP and H2-IOP, respectively). When comparing the level of change for each pressure setting between BPR deformer and BPR non-deformer, the difference was significant only for H2-IOP setting ($P = 0.029$). In all eyes, the absolute percentage of change was significantly higher than a threshold of 10% (H1-IOP: $P = 0.02$ and H2-IOP: $P = 0.004$).

Stress Analysis

Association slopes between BPR and strain values and strain range for the difference between baseline and high IOP setting and between H1-IOP and H2-IOP settings are reported in Table 2. A negative and significant association was noted for all pressure settings in all eyes and when BPR deformer and non-deformer were analyzed separately, with the exception of strain range for the H1-IOP versus H2-IOP setting. The negative association implies that a higher difference in BPR for the measurements at the baseline setting is associated with smaller strain. The magnitude of the association slopes was higher in the BPR deformed eyes compared to the BPR non-deformed eyes.

Discussion

In this study, we examined the in vivo, 3D deformation of the beams and pores of the LC in response to acute IOP modulation while maintaining fixed ICP in healthy non-human primate eyes. The main findings of our study are threefold; First, substantial inter-eye differences and various patterns exist in microstructural responses to IOP modulation. Second, in most eyes, the in vivo surface BPR deformation of the LC does not reflect the maximal deformation occurring within it and, therefore, has limited liability as an indicator of LC beam and pore deformation. Third, we characterized that in BPR non-deformer eyes the LC surface response may be used as an indicator of changes within it.

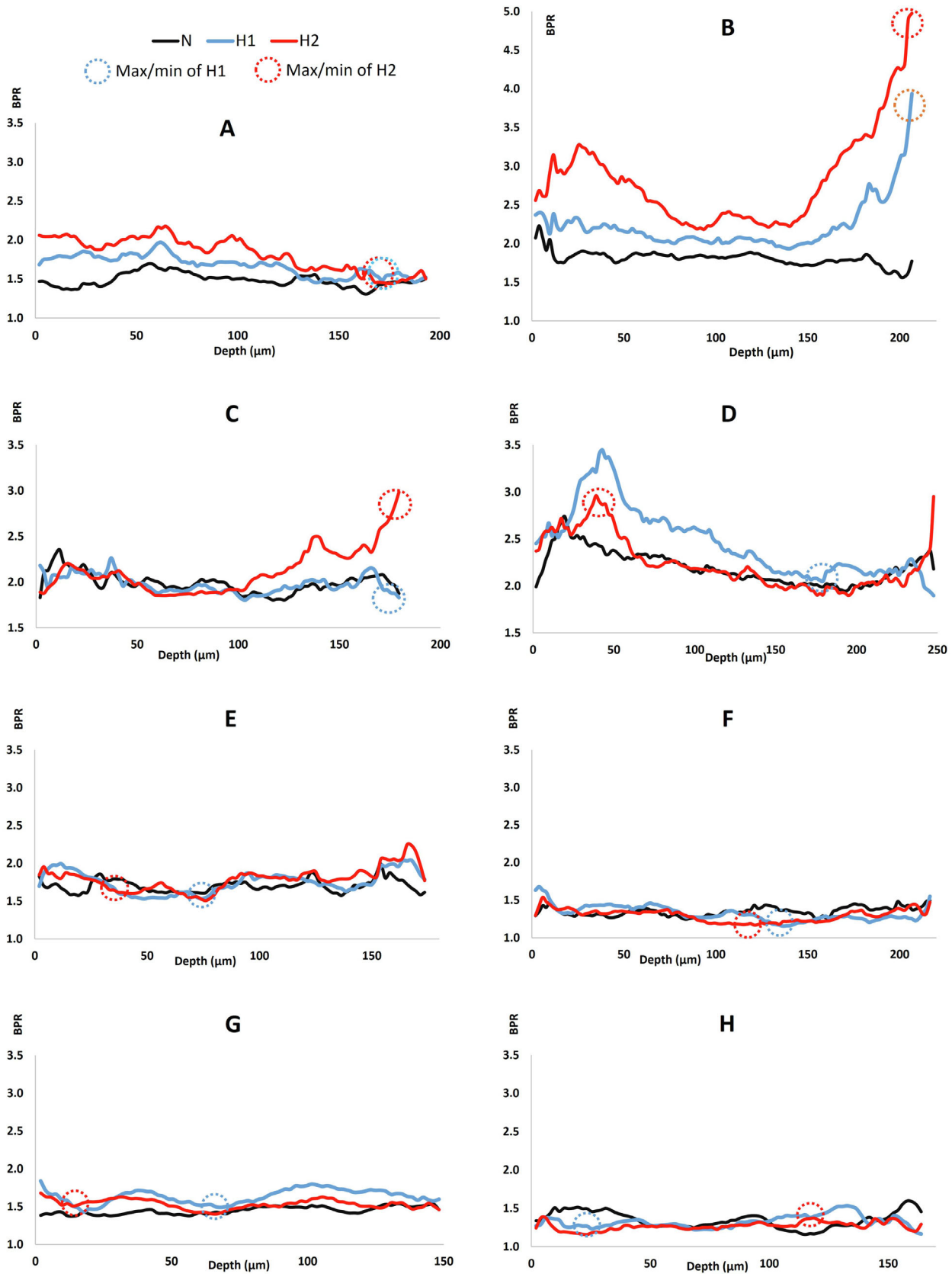

Figure 1. Anterior-to-posterior, lamina cribrosa beam-to-pore ratio (BPR) in response to acute IOP elevation in the presence of fixed intracranial pressure. The horizontal axis represents depth in microns. Points of maximum change (either positive or negative) from the anterior surface are marked with dashed circles and colored accordingly to the pressure setting. Eyes A to D exhibited substantial BPR deformation, whereas eyes E to H showed minimal change all through lamina depth. Marked variability is noted among eyes in response magnitude and location.

Investigative Ophthalmology & Visual Science

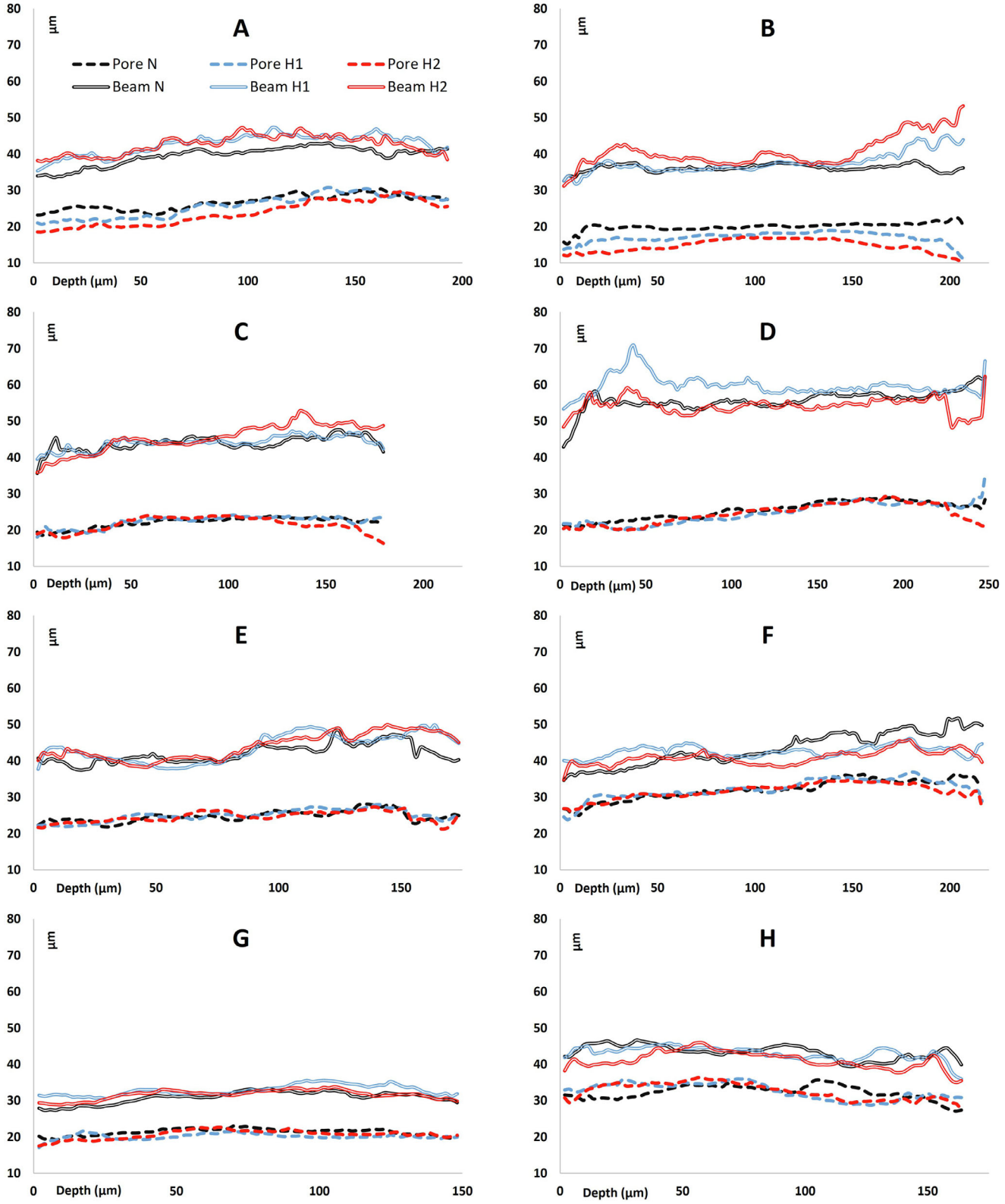

Figure 2. Anterior-to-posterior changes in beam thickness (*continuous lines*) and pore diameter (*dashed lines*) in all eyes in response to acute IOP elevation in the presence of fixed intracranial pressure. Both horizontal (depth) and vertical (thickness and diameter) axis units are in micrometers. Eyes are named in the same order, as reported in Figure 1 and Table 1.

Investigative Ophthalmology & Visual Science

Table 2. Association Between Difference in Beam-To-Pore Ratio (Δ BPR) and Strain Values and Strain Range Between Pressure Settings (N-IOP Against H1-IOP and H1-IOP Against H2-IOP) Calculated Using Mixed Effects Model Adjusted for Age

	N-IOP Versus H1-IOP		H1-IOP Versus H2-IOP	
	ΔBPR Versus Strain Values	ΔBPR Versus Strain Range	ΔBPR Versus Strain Values	ΔBPR Versus Strain Range
All eyes	**−6.44 (< 0.001)***	**−4.89 (< 0.001)***	**−5.59 (< 0.001)***	**−4.63 (< 0.001)***
BPR deformers	**−9.51 (< 0.001)***	**−8.05 (< 0.001)***	**−5.66 (< 0.001)***	**−4.84 (< 0.001)***
BPR non-deformers	**−4.39 (< 0.001)***	**−1.53 (0.020)***	**−4.29 (< 0.001)***	−0.40 (0.58)

* Statistically significant.

We have shown various patterns of LC beam and pore deformations in magnitude and location in response to IOP modulation: from relatively large magnitude anterior BPR deformation, moderate BPR deformation that is widely spread, deformation most pronounced in the posterior lamina, a combination of both anterior and posterior BPR deformation, or minimal deformation throughout. High variance in IOP-induced LC macrostructure response (the entire lamina and peripapillary scleral canal) was previously reported.[41,42] Our study provides novel information on the in vivo, depth-resolved, microstructural response when ICP is maintained at a fixed level. We have previously reported complex interaction between IOP and ICP in their effect on LC microstructure.[2] This study focuses on the IOP effect alone; thus, it is imperative to ensure that similar ICP levels are maintained across the pressure settings.

Eyes also varied in their response to the changing level of IOP modulation. Some eyes showed a linear BPR response to increasing IOP (higher IOP resulted in more significant BPR change), whereas others did not. For example, eyes A and B (see Fig. 1) showed a rise in BPR with each increase in IOP. However, eye C showed minimal BPR change between N and H1-IOP, whereas only H2-IOP evoked a posterior response. Eye D exhibited the maximal change with H1-IOP, whereas H2-IOP induced a lesser effect. A study regarding LC strains following a two-step IOP elevation reported that such diversity also exists in humans, in which responses were linear, nonlinear, or no response at all.[43] This marked variability in the lamina microstructure deformation can be attributed to inherent stiffness of the lamina, beam structure, and 3D orientation, or the composition of collagen and elastin within the beams that better resists pressure insult. Previous studies have also reported displacement of the LC in response to IOP modulation.[43–49] Our study was not designed for assessing displacement, as we registered the analyzed 3D location in scans obtained at different pressures.

When beam thickness and pore diameter effects were assessed separately, varying patterns were detected corresponding with the observed BPR reaction. In some instances, a decrease in pore diameter in response to pressure elevation was associated with an increase in beam thickness (see Figs. 2B, 2C, posteriorly). However, in others, a dissociation between the response of the two parameters was noted (see Figs. 2A, 2B anteriorly, 2C mid-depth). This multitude of responses has been previously shown in ex vivo studies,[41,50] and can be attributed to optic nerve opening expansion within the scleral canal or entire LC displacement. In a recent human and porcine ex vivo study, the anterior LC sustained higher strains than the posterior LC,[44] possibly due to its lower collagen content.[3]

The marked heterogeneity in BPR deformation patterns may result from natural diversity in connective tissue composition and property of the LC and the scleral canal.[51–53] This diversity might play an important role in glaucoma susceptibility or resistance.[51,54] LCs of subjects with ocular hypertension sustain lower strains than healthy eyes when exposed to elevated IOP attributed to the different connective tissue content of either the sclera or LC itself.[43] Age-related changes in the collagen content of the LC are also known to alter its biomechanical properties,[55,56] thus contributing to glaucoma susceptibility. Our cohort comprised only young adult animals with a limited age range, explaining why we did not detect a significant association between BPR deformation and age.

Comparing baseline LC characteristics between BPR deformers and non-deformers, we found that baseline pore AR was significantly higher in eyes that did not deform. A previous study that used enucleated sheep eyes reported that pore AR is positively correlated with peak tensile strain, proposing that elongated pores are more susceptible to mechanical insult.[57] Other studies on the relationship between pore shape and glaucomatous damage have shown conflicting evidence. Using OCT in vivo methodology, Wang et al. did not detect any association between pore AR and glaucoma.[18] However, more significant variance in pore shape was noticed in glaucomatous eyes compared to healthy controls.[18] Ivers et al. studied non-human primates with unilateral experimental glaucoma and did not detect any change in anterior surface pore elongation but did observe significant pore enlargement.[58] Two studies that used scanning laser ophthalmoscope reported conflicting information. Fontana et al. found a positive correlation between pore AR and glaucomatous damage,[59] whereas Akagi et al. did not detect such an association.[60] Of note, all three studies were limited by examining only the anterior LC surface, discounting possible deep LC changes.

Our study also showed that baseline CTVF was significantly higher in BPR deformer eyes compared to BPR non-deformers. Roberts et al. reported an increase in connective tissue volume in early experimental glaucoma, but that CTVF remained similar, as the volume of nonconnective tissue elements grew as well.[61] A biomechanical finite element model of healthy non-human primate eyes by the same group showed that CTVF positively correlated with Von Mises stress but negatively correlated with maximum principal strain.[62] Furthermore, we witnessed a trend in which eyes with higher baseline BPR were associated with a more IOP-induced deformation than eyes with low BPR. Higher BPR was previously associated with human glaucomatous eyes and decreasing mean deviation, thought to be caused by remodeling-associated beam thickening and axonal loss, resulting in smaller pores.[18] This discrepancy

Investigative Ophthalmology & Visual Science

can be explained by the use of healthy animals in our study who were not affected by remodeling. Accordingly, the average BPR in our study was comparable to the healthy group in the cited study.[18] Our finding implies that in eyes with low BPR, analysis of the anterior lamina might be more reflective of the response of the entire lamina. The association between baseline BPR and the risk of glaucoma should be examined in future studies.

Changes in BPR in response to IOP modulation when compared to baseline in each plane, are reduced with depth. As the IOP force is primarily in the anterior-posterior direction, it can be expected that, in the presence of a fixed ICP, the further from the origin of the force (anterior lamina surface) the effect on the tissue will dissolve. Interestingly, in the model, the effect of depth was stronger (−0.0011) and with substantially lower P value ($<2e^{-16}$) in the high IOP modulation setting compared to the very high setting (−0.0003 and $P = 0.008$, respectively). This finding might indicate that the lamina reached its maximal deformation level around 30 mm Hg and afterward it becomes stiffer and deforms to a lesser extent, which is in agreement with a previous ex vivo study.[63]

Numerous in vivo studies on the LC, both on micro- and macrostructure, focus mainly on the anterior LC surface to understand the pathophysiology of glaucoma, distinguishing between healthy and glaucoma, and predicting the disease behavior.[29,30,64] Our results clearly indicate that substantial microstructural deformations occur within the lamina depth and are not associated with changes detected in the anterior surface. We have shown that all eyes exhibited deformations that exceeded an absolute 10% change from the anterior LC surface. A 10% threshold was selected as past in vitro studies have shown that a 10% to 20% stretch may lead to neuronal damage and astrocyte activation.[65–67] Considering that the axons passing through the entire LC volume on their way from the retina to the brain, assessing only its anterior surface is insufficient in determining the risk and location of mechanical stress-induced damage. It is therefore recommended to evaluate the entire LC volume in the context of glaucoma.

Our stress analysis showed that higher BPR change is associated with lower strain values and strain range (see Table 2). We also observed that, in the BPR deformer eyes, the association with strain was steeper compared with the BPR non-deformers. These indicate that eyes that deform, according to the change in BPR, are less prone to the effect of strain and thus "absorb" some of the effects of increased IOP, whereas BPR non-deformer eyes experience higher strain which might lead to axonal damage. Further in vivo investigation is warranted.

Several limitations should be considered when evaluating the results of our study. Visibility of the LC is inevitably limited by superficial vasculature in OCT in vivo imaging. Additionally, we have previously demonstrated significant sectoral variability in human LC imaging.[19] Therefore, we ensured to use the common analyzable LC among all the pressure settings in each eye for high fidelity, which further reduced the overall analyzed region. This inescapable limitation of the OCT technology is partially mitigated by pooling data across eyes where the analyzable area varies to allow coverage of larger areas of the lamina. Second, the spectral-domain OCT signal is attenuated in depth, which might reduce the reliability of our findings in the posterior lamina. Nevertheless, our results were mostly consistent in the different scans acquired in the various pressure settings improving the confidence in our conclusions. Third, the BoneJ algorithm has an inherent limitation in which larger pores are over-represented in the overall measured average as they include more voxels. Considering that our primary outcome is a ratio (BPR), its overall impact is minimal. Note that this limitation did not affect volumetric parameters, such as CTVF, where the absolute count of voxels within the segmented beams was used. Last, the cross-sectional nature of this experiment does not consider the remodeling process occurring in glaucoma. Moreover, our analysis considers only structural deformations and not functional nor dynamic strain forces. However, our results set the foundation for future studies to evaluate these aspects.

In conclusion, as the pattern and location of in vivo lamina BPR deformation vary substantially among eyes in response to acute IOP modulation while maintaining fixed ICP, the entire lamina should be analyzed in studies associated with glaucoma. The pathophysiological implication of the different responses warrants further investigation.

Acknowledgments

The authors would like to thank MA Smith, and S Schmitt, BS, from the Department of Biomedical Engineering and Neuroscience Institute, Carnegie Mellon University, Pittsburgh, PA, for their assistance in animal handling.

Financial Support: NIH R01-EY030770, R01-EY025011, R01-EY013178 (Bethesda, MD), and an unrestricted grant from Research to Prevent Blindness (New York, NY).

Disclosure: **Y. Glidai**, None; **K.A. Lucy**, None; **J.S. Schuman**, receives royalties for intellectual property licensed by the Massachusetts Institute of Technology and Massachusetts Eye and Ear Infirmary to Zeiss; **P. Alexopoulos**, None; **B. Wang**, None; **M. Wu**, None; **M. Liu**, None; **J.P. Vande Geest**, None; **H.G. Kollech**, None; **T. Lee**, None; **H. Ishikawa**, None; **G. Wollstein**, None

References

1. Jonas JB, Kutscher JN, Panda-Jonas S, Hayreh SS. Lamina cribrosa thickness correlated with posterior scleral thickness and axial length in monkeys. *Acta Ophthalmol*. 2016;94:e693–e696.
2. Wang B, Tran H, Smith MA, et al. In-vivo effects of intraocular and intracranial pressures on the lamina cribrosa microstructure. *PLoS One*. 2017;12:e0188302.
3. Elkington AR, Inman CB, Steart PV, Weller RO. The structure of the lamina cribrosa of the human eye: an immunocytochemical and electron microscopical study. *Eye*. 1990;4(Pt 1):42–57.
4. Radius RL, Gonzales M. Anatomy of the lamina cribrosa in human eyes. *Arch Ophthalmol (Chicago, Ill: 1960)*. 1981;99:2159–2162.
5. Anderson DR. Ultrastructure of human and monkey lamina cribrosa and optic nerve head. *Arch Ophthalmol (Chicago, Ill: 1960)*. 1969;82:800–814.
6. Quigley HA, Addicks EM, Green WR, Maumenee AE. Optic nerve damage in human glaucoma. II. The site of injury and susceptibility to damage. *Arch Ophthalmol (Chicago, Ill: 1960)*. 1981;99:635–649.
7. Burgoyne CF. A biomechanical paradigm for axonal insult within the optic nerve head in aging and glaucoma. *Exp Eye Res*. 2011;93:120–132.
8. Quigley H, Anderson DR. The dynamics and location of axonal transport blockade by acute intraocular

pressure elevation in primate optic nerve. *Invest Ophthalmol*. 1976;15:606–616.
9. Downs JC, Girkin CA. Lamina cribrosa in glaucoma. *Curr Opin Ophthalmol*. 2017;28:113–119.
10. Wilczek M. The lamina cribrosa and its nature. *Br J Ophthalmol*. 1947;31:551–565.
11. Vurgese S, Panda-Jonas S, Jonas JB. Scleral thickness in human eyes. *PLoS One*. 2012;7:e29692.
12. Quigley HA, Hohman RM, Addicks EM, Massof RW, Green WR. Morphologic changes in the lamina cribrosa correlated with neural loss in open-angle glaucoma. *Am J Ophthalmol*. 1983;95:673–691.
13. Hernandez MR, Ye H. Glaucoma: changes in extracellular matrix in the optic nerve head. *Ann Med*. 1993;25:309–315.
14. Downs JC, Roberts MD, Sigal IA. Glaucomatous cupping of the lamina cribrosa: a review of the evidence for active progressive remodeling as a mechanism. *Exp Eye Res*. 2011;93:133–140.
15. Burgoyne CF, Downs JC, Bellezza AJ, Suh JK, Hart RT. The optic nerve head as a biomechanical structure: a new paradigm for understanding the role of IOP-related stress and strain in the pathophysiology of glaucomatous optic nerve head damage. *Prog Retin Eye Res*. 2005;24:39–73.
16. Tan NY, Koh V, Girard MJ, Cheng CY. Imaging of the lamina cribrosa and its role in glaucoma: a review. *Clin Exp Ophthalmol*. 2018;46:177–188.
17. Kagemann L, Ishikawa H, Wollstein G, et al. Ultrahigh-resolution spectral domain optical coherence tomography imaging of the lamina cribrosa. *Ophthalmic Surg Lasers Imaging*. 2008;39:S126–S131.
18. Wang B, Nevins JE, Nadler Z, et al. In vivo lamina cribrosa micro-architecture in healthy and glaucomatous eyes as assessed by optical coherence tomography. *Invest Ophthalmol Vis Sci*. 2013;54:8270–8274.
19. Nadler Z, Wang B, Schuman JS, et al. In vivo three-dimensional characterization of the healthy human lamina cribrosa with adaptive optics spectral-domain optical coherence tomography. *Invest Ophthalmol Vis Sci*. 2014;55:6459–6466.
20. Midgett DE, Pease ME, Jefferys JL, et al. The pressure-induced deformation response of the human lamina cribrosa: Analysis of regional variations. *Acta Biomaterialia*. 2017;53:123–139.
21. Chien JL, Ghassibi MP, Mahadeshwar P, et al. A Novel Method for Assessing Lamina Cribrosa Structure Ex Vivo Using Anterior Segment Enhanced Depth Imaging Optical Coherence Tomography. *J Glaucoma*. 2017;26:626–632.
22. Naranjo-Bonilla P, Gimenez-Gomez R, Rios-Jimenez D, et al. Enhanced depth OCT imaging of the lamina cribrosa for 24 hours. *Int J Ophthalmol*. 2017;10:306–309.
23. Park SC, De Moraes CG, Teng CC, Tello C, Liebmann JM, Ritch R. Enhanced depth imaging optical coherence tomography of deep optic nerve complex structures in glaucoma. *Ophthalmology*. 2012;119:3–9.
24. Park HY, Jeon SH, Park CK. Enhanced depth imaging detects lamina cribrosa thickness differences in normal tension glaucoma and primary open-angle glaucoma. *Ophthalmology*. 2012;119:10–20.
25. Kim M, Bojikian KD, Slabaugh MA, Ding L, Chen PP. Lamina depth and thickness correlate with glaucoma severity. *Indian J Ophthalmol*. 2016;64:358–363.
26. Thitiwichienlert S, Ishikawa H, Asakawa K, Ikeda T, Shimizu K. Enhanced Depth Imaging of Central Laminar Thickness in Optic Neuropathy: Comparison with Normal Eyes. *Neuro-Ophthalmology (Aeolus Press)*. 2015;39:166–174.
27. Park SC, Brumm J, Furlanetto RL, et al. Lamina cribrosa depth in different stages of glaucoma. *Invest Ophthalmol Vis Sci*. 2015;56:2059–2064.
28. Prata TS, Lopes FS, Prado VG, et al. In vivo analysis of glaucoma-related features within the optic nerve head using enhanced depth imaging optical coherence tomography. *PLoS One*. 2017;12:e0180128.
29. Furlanetto RL, Park SC, Damle UJ, et al. Posterior displacement of the lamina cribrosa in glaucoma: in vivo interindividual and intereye comparisons. *Invest Ophthalmol Vis Sci*. 2013;54:4836–4842.
30. Lee SH, Kim TW, Lee EJ, Girard MJ, Mari JM. Diagnostic Power of Lamina Cribrosa Depth and Curvature in Glaucoma. *Invest Ophthalmol Vis Sci*. 2017;58:755–762.
31. Kim YW, Jeoung JW, Girard MJ, Mari JM, Park KH. Positional and Curvature Difference of Lamina Cribrosa According to the Baseline Intraocular Pressure in Primary Open-Angle Glaucoma: A Swept-Source Optical Coherence Tomography (SS-OCT) Study. *PLoS One*. 2016;11:e0162182.
32. Kim YW, Jeoung JW, Kim DW, et al. Clinical Assessment of Lamina Cribrosa Curvature in Eyes with Primary Open-Angle Glaucoma. *PLoS One*. 2016;11:e0150260.
33. Oh BL, Lee EJ, Kim H, Girard MJ, Mari JM, Kim TW. Anterior Lamina Cribrosa Surface Depth in Open-Angle Glaucoma: Relationship with the Position of the Central Retinal Vessel Trunk. *PLoS One*. 2016;11:e0158443.
34. Ha A, Kim TJ, Girard MJA, et al. Baseline Lamina Cribrosa Curvature and Subsequent Visual Field Progression Rate in Primary Open-Angle Glaucoma. *Ophthalmology*. 2018;125:1898–1906.
35. Downs JC, Suh JK, Thomas KA, Bellezza AJ, Hart RT, Burgoyne CF. Viscoelastic material properties of the peripapillary sclera in normal and early-glaucoma monkey eyes. *Invest Ophthalmol Vis Sci*. 2005;46:540–546.
36. Nadler Z, Wang B, Wollstein G, et al. Automated lamina cribrosa microstructural segmentation in optical coherence tomography scans of healthy and glaucomatous eyes. *Biomed Opt Express*. 2013;4:2596–2608.
37. Behkam R, Kollech HG, Jana A, et al. Racioethnic differences in the biomechanical response of the lamina cribrosa. *Acta Biomater*. 2019;88:131–140.
38. Thirion JP. Image matching as a diffusion process: an analogy with Maxwell's demons. *Med Image Anal*. 1998;2:243–260.
39. Kroon D-J. *B-spline Grid, Image and Point based Registration*. MATLAB Central File Exchange; 2022. Available at: https://www.mathworks.com/matlabcentral/fileexchange/74112-flow2d/?msclkid=7f5db12bd14611ec90aca0a773d-26dce.
40. Abd-Elmoniem KZ, Stuber M, Prince JL. Direct three-dimensional myocardial strain tensor quantification and tracking using zHARP. *Med Image Anal*. 2008;12:778–786.
41. Yang H, Downs JC, Sigal IA, Roberts MD, Thompson H, Burgoyne CF. Deformation of the normal monkey optic nerve head connective tissue after acute IOP elevation within 3-D histomorphometric reconstructions. *Invest Ophthalmol Vis Sci*. 2009;50:5785–5799.
42. Sigal IA, Yang H, Roberts MD, Burgoyne CF, Downs JC. IOP-induced lamina cribrosa displacement and scleral canal expansion: an analysis of factor interactions using parameterized eye-specific models. *Invest Ophthalmol Vis Sci*. 2011;52:1896–1907.
43. Beotra MR, Wang X, Tun TA, et al. In Vivo Three-Dimensional Lamina Cribrosa Strains in Healthy, Ocular Hypertensive, and Glaucoma Eyes Following Acute Intraocular Pressure Elevation. *Invest Ophthalmol Vis Sci*. 2018;59:260–272.
44. Ma Y, Pavlatos E, Clayson K, et al. Mechanical Deformation of Human Optic Nerve Head and Peripapillary Tissue in Response to Acute IOP Elevation. *Invest Ophthalmol Vis Sci*. 2019;60:913–920.

Investigative Ophthalmology & Visual Science

45. Midgett DE, Quigley HA, Nguyen TD. In vivo characterization of the deformation of the human optic nerve head using optical coherence tomography and digital volume correlation. *Acta Biomaterialia*. 2019;96:385–399.
46. Agoumi Y, Sharpe GP, Hutchison DM, Nicolela MT, Artes PH, Chauhan BC. Laminar and prelaminar tissue displacement during intraocular pressure elevation in glaucoma patients and healthy controls. *Ophthalmology*. 2011;118:52–59.
47. Morgan WH, Chauhan BC, Yu DY, Cringle SJ, Alder VA, House PH. Optic disc movement with variations in intraocular and cerebrospinal fluid pressure. *Invest Ophthalmol Vis Sci*. 2002;43:3236–3242.
48. Quigley H, Arora K, Idrees S, et al. Biomechanical Responses of Lamina Cribrosa to Intraocular Pressure Change Assessed by Optical Coherence Tomography in Glaucoma Eyes. *Invest Ophthalmol Vis Sci*. 2017;58:2566–2577.
49. Fazio MA, Johnstone JK, Smith B, Wang L, Girkin CA. Displacement of the Lamina Cribrosa in Response to Acute Intraocular Pressure Elevation in Normal Individuals of African and European Descent. *Invest Ophthalmol Vis Sci*. 2016;57:3331–3339.
50. Sigal IA, Grimm JL, Jan NJ, Reid K, Minckler DS, Brown DJ. Eye-specific IOP-induced displacements and deformations of human lamina cribrosa. *Invest Ophthalmol Vis Sci*. 2014;55:1–15.
51. Tengroth B, Ammitzboll T. Changes in the content and composition of collagen in the glaucomatous eye–basis for a new hypothesis for the genesis of chronic open angle glaucoma–a preliminary report. *Acta Ophthalmol (Copenh)*. 1984;62:999–1008.
52. Yang H, Downs JC, Burgoyne CF. Physiologic intereye differences in monkey optic nerve head architecture and their relation to changes in early experimental glaucoma. *Invest Ophthalmol Vis Sci*. 2009;50:224–234.
53. Karimi A, Rahmati SM, Grytz RG, Girkin CA, Downs JC. Modeling the biomechanics of the lamina cribrosa microstructure in the human eye. *Acta Biomaterialia*. 2021;134:357–378.
54. Huang W, Fan Q, Wang W, Zhou M, Laties AM, Zhang X. Collagen: a potential factor involved in the pathogenesis of glaucoma. *Med Sci Monit Basic Res*. 2013;19:237–240.
55. Hernandez MR, Luo XX, Andrzejewska W, Neufeld AH. Age-related changes in the extracellular matrix of the human optic nerve head. *Am J Ophthalmol*. 1989;107:476–484.
56. Albon J, Karwatowski WS, Easty DL, Sims TJ, Duance VC. Age related changes in the non-collagenous components of the extracellular matrix of the human lamina cribrosa. *Br J Ophthalmol*. 2000;84:311–317.
57. Voorhees AP, Jan NJ, Austin ME, et al. Lamina Cribrosa Pore Shape and Size as Predictors of Neural Tissue Mechanical Insult. *Invest Ophthalmol Vis Sci*. 2017;58:5336–5346.
58. Ivers KM, Sredar N, Patel NB, et al. In Vivo Changes in Lamina Cribrosa Microarchitecture and Optic Nerve Head Structure in Early Experimental Glaucoma. *PLoS One*. 2015;10:e0134223.
59. Fontana L, Bhandari A, Fitzke FW, Hitchings RA. In vivo morphometry of the lamina cribrosa and its relation to visual field loss in glaucoma. *Curr Eye Res*. 1998;17:363–369.
60. Akagi T, Hangai M, Takayama K, Nonaka A, Ooto S, Yoshimura N. In vivo imaging of lamina cribrosa pores by adaptive optics scanning laser ophthalmoscopy. *Invest Ophthalmol Vis Sci*. 2012;53:4111–4119.
61. Roberts MD, Grau V, Grimm J, et al. Remodeling of the connective tissue microarchitecture of the lamina cribrosa in early experimental glaucoma. *Invest Ophthalmol Vis Sci*. 2009;50:681–690.
62. Roberts MD, Liang Y, Sigal IA, et al. Correlation between local stress and strain and lamina cribrosa connective tissue volume fraction in normal monkey eyes. *Invest Ophthalmol Vis Sci*. 2010;51:295–307.
63. Jan NJ, Gomez C, Moed S, et al. Microstructural Crimp of the Lamina Cribrosa and Peripapillary Sclera Collagen Fibers. *Invest Ophthalmol Vis Sci*. 2017;58:3378–3388.
64. Thakku SG, Tham YC, Baskaran M, et al. A Global Shape Index to Characterize Anterior Lamina Cribrosa Morphology and Its Determinants in Healthy Indian Eyes. *Invest Ophthalmol Vis Sci*. 2015;56:3604–3614.
65. Salvador E, Burek M, Förster CY. Stretch and/or oxygen glucose deprivation (OGD) in an in vitro traumatic brain injury (TBI) model induces calcium alteration and inflammatory cascade. *Front Cell Neurosci*. 2015;9:323.
66. Kirwan RP, Fenerty CH, Crean J, Wordinger RJ, Clark AF, O'Brien CJ. Influence of cyclical mechanical strain on extracellular matrix gene expression in human lamina cribrosa cells in vitro. *Mol Vis*. 2005;11:798–810.
67. Rogers RS, Dharsee M, Ackloo S, Sivak JM, Flanagan JG. Proteomics analyses of human optic nerve head astrocytes following biomechanical strain. *Mol Cell Proteomics*. 2012;11:M111.012302.

Investigative Ophthalmology & Visual Science